

JGR Solid Earth

RESEARCH ARTICLE

10.1029/2023JB026529

Key Points:

- Broadband Rayleigh-wave dispersion array analysis has been conducted in the oldest (~170 Ma) Pacific seafloor
- The low-velocity zone is significantly slower to indicate the occurrence of some reheating process beneath the oldest Pacific lithosphere
- The spatial variation of the shallow azimuthal anisotropy indicates a complicated evolution of the infant Pacific plate

Supporting Information:

Supporting Information may be found in the online version of this article.

Correspondence to:

T. Isse,
tisse@eri.u-tokyo.ac.jp

Citation:

Kawano, Y., Isse, T., Takeo, A., Kawakatsu, H., Morishige, M., Shiobara, H., et al. (2023). Seismic structure of the lithosphere–asthenosphere system beneath the oldest seafloor revealed by Rayleigh-wave dispersion analysis. *Journal of Geophysical Research: Solid Earth*, 128, e2023JB026529. <https://doi.org/10.1029/2023JB026529>

Received 10 FEB 2023

Accepted 2 JUN 2023

Author Contributions:

Conceptualization: Hitoshi Kawakatsu, Hisashi Utada, Sang-Mook Lee

Data curation: Takehi Isse, Hajime Shiobara

Formal analysis: Yuki Kawano, Manabu Morishige

Funding acquisition: Yuki Kawano, Takehi Isse, Hitoshi Kawakatsu, Nozomu Takeuchi, YoungHee Kim, Hisashi Utada, Sang-Mook Lee

Investigation: Takehi Isse, Hajime Shiobara, Hiroko Sugioka, YoungHee Kim

Methodology: Yuki Kawano, Akiko Takeo, Manabu Morishige

© 2023. The Authors.

This is an open access article under the terms of the Creative Commons Attribution License, which permits use, distribution and reproduction in any medium, provided the original work is properly cited.

Seismic Structure of the Lithosphere–Asthenosphere System Beneath the Oldest Seafloor Revealed by Rayleigh-Wave Dispersion Analysis

Yuki Kawano¹ , Takehi Isse¹ , Akiko Takeo¹ , Hitoshi Kawakatsu^{1,2} , Manabu Morishige¹ , Hajime Shiobara¹ , Nozomu Takeuchi¹ , Hiroko Sugioka³ , YoungHee Kim⁴ , Hisashi Utada¹ , and Sang-Mook Lee⁴ 

¹Earthquake Research Institute, The University of Tokyo, Tokyo, Japan, ²Institute of Earth Sciences, Academia Sinica, Taipei, Taiwan, ³Graduate School of Science, Kobe University, Hyogo, Japan, ⁴School of Earth and Environmental Sciences, Seoul National University, Seoul, Republic of Korea

Abstract We analyze seismic records collected at the oldest (170–180 Ma) Pacific seafloor using broadband dispersion array analysis. Using ambient noise and teleseismic waveforms, we measure Rayleigh-wave phase velocities in a period range of 5–200 s that are inverted for array-average one-dimensional isotropic and azimuthally anisotropic shear-wave velocity depth profiles from the crust to a depth of 300 km. The high-velocity Lid and the low-velocity zone are well-resolved with velocity difference of ~4%, whose transition occurs at depths between 80 and 100 km. The profile is compared with that obtained at the 130- and 140-Ma seafloor. Accounting for the cooling effect due to the plate age difference, the low-velocity zone of the oldest Pacific seafloor is ~1.3% slower (~110°C warmer) than that beneath the 140-Ma seafloor, suggesting the occurrence of some reheating process beneath the oldest lithosphere. The azimuthal anisotropy at shallow depths (<50 km) is significantly different between the western and eastern areas of the array where the peak-to-peak amplitudes are estimated to be ~2.8% and ~1.6%, respectively. The fast direction is nearly parallel to the past seafloor spreading direction (perpendicular to the magnetic lineation) in the west, while it largely deviates in the east. The observed difference in azimuthal anisotropy may represent complicated evolution dynamics of the infant Pacific plate that involved a ridge–ridge–ridge triple junction.

Plain Language Summary One of the classical enigmas of plate tectonics is the cause of seafloor flattening where the seafloor depth becomes nearly constant for old ages (>~70 Ma) while a simple cooling model of plate evolution predicts the age dependence. To solve this enigma, it is essential to resolve the subsurface structure of the oceanic plate and the asthenosphere below. As a part of an international effort, Pacific Array, that aims to cover the Pacific seafloor by arrays of ocean bottom seismometers, a team of Japanese and Korean scientists deployed an array in the oldest (170–180 Ma) Pacific seafloor. We determine isotropic and anisotropic shear-wave velocity structures as a first step toward resolving the enigma. The results indicate that the asthenosphere beneath the oldest Pacific lithosphere is significantly slower than the prediction of the simple cooling and that the occurrence of some reheating process may be needed. Furthermore, azimuthal anisotropy (the dependence of the wave velocity on the horizontal propagation direction) in the shallow lithosphere shows that the anisotropy patterns differ between the eastern and western areas of the array, and simulation results indicate that the evolution process of the infant Pacific plate is not merely a simple triangular plate spreading.

1. Introduction

With the short thermo-chemical evolution history, seismic imaging of the oceanic crust and mantle is essential to elucidate the nature of the lithosphere–asthenosphere system (LAS). The typical oceanic LAS consists of a thin crust with a thickness of ~7 km (White et al., 1992), a high-velocity layer (Lid) in a depth range of ~30–~80 km, and an underlying low-velocity zone (LVZ) down to a depth of ~200 km (Dorman et al., 1960; Gutenberg, 1948; Gutenberg & Richter, 1939; Nishimura & Forsyth, 1989). The oceanic plate emerges at the mid-oceanic ridge, and as it moves away horizontally, the plate cools and thickens, eventually sinking back into the mantle at the subduction zone.

Project Administration: Nozomu Takeuchi, YoungHee Kim, Hisashi Utada, Sang-Mook Lee

Software: Yuki Kawano, Akiko Takeo, Manabu Morishige

Supervision: Takehi Isse, Akiko Takeo, Hitoshi Kawakatsu

Visualization: Yuki Kawano, Manabu Morishige

Writing – original draft: Yuki Kawano, Takehi Isse, Akiko Takeo, Hitoshi Kawakatsu, Manabu Morishige

Writing – review & editing: YoungHee Kim, Hisashi Utada

As a first order approximation, the evolution of oceanic mantle can be explained by a simple thermal diffusion. At ages younger than 70 Ma, the age dependence of bathymetry and heat flow data can be explained by a half-space cooling (HSC) model, which assumes that the plate cools and thickens by heat conduction in the vertical direction and subsides due to its own weight (e.g., Parker & Oldenburg, 1973). Seismic tomography has shown that the Lid becomes thicker, and the seismic velocity in the LVZ becomes faster beneath the older seafloor, indicating that the change in the thermal structure due to cooling with age is a primary factor controlling the seismic velocity structure of the oceanic LAS (e.g., Maggi et al., 2006a). Due to the observed strong correlation between the seafloor age and the Lid/LVZ structure, the Lid and LVZ are often associated with the lithosphere and the asthenosphere, respectively.

At ages greater than 70 Ma, however, it is known that the depth of seafloor is significantly shallower (the seafloor flattening) and the heat flow is higher than those of the HSC model predictions (e.g., Parsons & Sclater, 1977; Stein & Stein, 1992). An empirical model with a thermal boundary at a depth, the plate-cooling model, explains bathymetry and heat flow data (e.g., Parsons & Sclater, 1977; Stein & Stein, 1992). However, what kind of structure corresponds to the thermal boundary is ambiguous and has long been under debate. Sub-lithospheric small-scale convection (SSC) has been proposed as a candidate (e.g., Parsons & McKenzie, 1978; Richter & Parsons, 1975), and the recent Pacific seafloor array deployments have started to reveal such signatures (Eilon et al., 2022; Takeo et al., 2018). Meanwhile, alternative models attributing to other mechanisms, such as asthenospheric reheating (e.g., Utada, 2019) or Earth's secular cooling and radiogenic heating (Korenaga et al., 2021) have also been proposed.

Broadband dispersion array analysis is a powerful tool for quantitatively investigating the oceanic LAS (Takeo et al., 2013). Ambient noise and teleseismic waveforms are used to measure broadband dispersion curves that are then inverted for a continuous depth profile of seismic velocities from crust to the depths within the asthenosphere. The obtained depth profile reflects the structure directly beneath the array of broadband ocean bottom seismometers (BBOBSs) with a higher spatial resolution compared to the global tomography. Such analyses have been conducted at the Pacific seafloors of various ages (Lin et al., 2016; Russell, 2021; Russell et al., 2019; Takeo et al., 2013, 2016, 2018; Yang et al., 2020).

The shearing associated with the seafloor spreading and the subsequent plate motion produces a lattice preferred orientation (LPO) of olivine crystals with the fast axis oriented in the shear direction, resulting in the azimuthal anisotropy of velocities of elastic waves (e.g., Karato et al., 2008). Lithospheric azimuthal anisotropy is conventionally interpreted as a proxy of mantle shearing due to the past seafloor spreading (e.g., Nicolas & Christensen, 1987). Seismic azimuthal anisotropy with its fast direction perpendicular to magnetic lineation is frequently observed for both body and surface waves (e.g., Forsyth, 1975; Hess, 1964; Lin et al., 2016; Mark et al., 2019; Takeo et al., 2014), whereas there are also observations of the fast directions that are oblique to the magnetic lineation, which may challenge the conventional notion (e.g., Shintaku et al., 2014; Takeo et al., 2016, 2018; Toomey et al., 2007).

Within the asthenosphere, the fast direction of azimuthal anisotropy is generally coherent with the absolute plate motion (APM) (e.g., Burgos et al., 2014; Maggi et al., 2006b). The coherent relationships are interpreted as flow-induced LPO alignment, resulting from the shearing associated with the recent plate motions. However, recent broadband dispersion array analyses observed the fast directions, which significantly deviated from the APM and are interpreted as the result of disturbances caused by small-scale thermal convection or other mechanisms in the LVZ (Lin et al., 2016; Russell, 2021; Russell et al., 2019; Takeo et al., 2018).

In this study, we analyze the seismic data recorded at the oldest (170–180 Ma) Pacific seafloor. We apply the broadband dispersion array analysis using Rayleigh waves and obtain array average one-dimensional isotropic and azimuthally anisotropic shear-wave velocity (β_v) profiles, where β_v is the velocity of horizontally propagating vertically polarized shear waves.

2. Study Area and Data: The Oldest-1 Array

We analyze the seafloor seismic records obtained by an array deployed along the 170- and 180-Ma isochrons in the western Pacific, the Oldest-1 Array (Figure 1). The array consists of eleven BBOBSs, twelve differential pressure gauges (DPGs), and seven ocean bottom electro-magnetometers (OBEMs), and is operated from November 2018 to November 2019 as a Japan–South Korea collaborated research within the Pacific Array

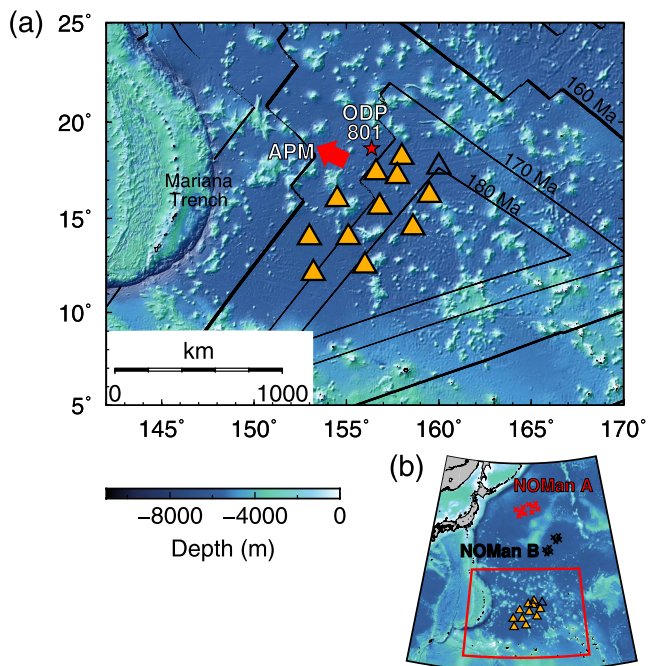


Figure 1. (a) Location map of the Oldest-1 Array. The orange-filled triangles represent the broadband ocean bottom seismometer (BBOBS) stations with differential pressure gauge (DPG) equipped, and the black open triangle represents the DPG station. The thin black lines represent isochrones by Seton et al. (2020), the red thick arrow represents the current absolute plate motion (APM), and the red star represents the ODP site 801 of Leg 129 (Abrams et al., 1993). (b) Regional map showing the locations of the recent BBOBS arrays in the western Pacific. The area of the red box is shown in (a). The red and black crosses represent the locations of the arrays of NOMan A and B (Takeo et al., 2018), respectively.

initiative framework (<http://eri-ndc.eri.u-tokyo.ac.jp/PacificArray/>). It is designed to unravel the lithosphere–asthenosphere system beneath the oldest Pacific seafloor, with a particular focus on the evolution process of the infant Pacific plate and the current sub-lithospheric dynamics that are related to the seafloor flattening phenomena. Results from the OBEM array analyses will be reported separately.

The marine magnetic lineations indicate that the oldest seafloor lies in the western-central Pacific (Larson & Chase, 1972). The area surrounded by Chron M29 (~160 Ma) is known to be characterized by low-amplitude and uncorrelated magnetic anomalies (Nakanishi et al., 1992). Partly because the magnetic lineation is not clearly observable at the old seafloor (>160–170 Ma), the early evolutionary process of the Pacific plate during the Jurassic (~145–200 Ma) remains poorly understood. The oldest seafloor is known to have experienced the subsequent Cretaceous volcanic activity (e.g., Koppers et al., 2003). Most drilling and dredging experiments sampled Cretaceous rocks, except for the ODP Site 801 (Figure 1a) of Leg 129 that recovered Jurassic oceanic crust aging 166.8 ± 4.5 million years (Myrs) (Abrams et al., 1993).

Abrams et al. (1993) reported the first results of the multichannel seismic studies whose study region includes the Oldest-1 Array region. They obtained one-dimensional depth profiles of compressional-wave (P-wave) velocity in the southwestern and northeastern parts of the Oldest-1 Array region. The total crustal thickness was between ~7–8 km, and subsequent studies obtained consistent results in the northeastern part of the Oldest-1 Array (Kaneda et al., 2010; Stadler & Tominaga, 2015). Abrams et al. (1993) observed no seismically resolvable systematic differences both in crustal thickness and in P-wave velocity between the southwestern and northeastern areas. Furthermore, the depth profiles were consistent with the normal oceanic crustal structure (Abrams et al., 1993), except for survey results in the vicinity of seamounts. The thickness of middle Cretaceous igneous sills/flows that overlay the Jurassic oceanic crust is estimated to be 400 m maximum (Abrams et al., 1993).

3. Broadband Rayleigh-Wave Dispersion Measurement

3.1. Tilt- and Compliance-Noise Removal

We remove the tilt and compliance noise from the long-period vertical component seismograms recorded by BBOBSs. The tilt noise originates from the seafloor current, causing gravitational acceleration recorded in the horizontal components that can be quite large. The imperfect leveling of a seismic sensor (i.e., the misalignment of the sensor's vertical axis from the gravitational direction), which is often unavoidable under the seafloor observation environment, further maps the tilt noise into the vertical component, resulting in strong noise in the vertical component that is coherent with the horizontal tilt noise (Crawford & Webb, 2000). We estimate the time-invariant and frequency-independent noise transfer function from the horizontal to the vertical by analyzing the records and remove the coherent horizontal noise from the vertical component seismograms in time domain (the detail can be found in a separate publication, Kawano et al., 2023). We further remove the compliance noise, which originates from the pressure loading on the seafloor due to infragravity waves, in the vertical component seismograms at a period range of 50–500 s following the conventional approach using the associated DPG data (e.g., Bell et al., 2015; Crawford & Webb, 2000). Noise-reduced vertical component seismograms are quieter by up to 20 dB than original seismograms at periods longer than 30 s (Kawano et al., 2023).

3.2. Broadband Surface-Wave Array Analysis

We use ambient noise and teleseismic event waveforms to measure broadband (5–200 s) Rayleigh-wave phase velocities. Here we briefly describe the method, focusing on the procedures that differ from the previous studies (Takeo et al., 2013, 2016, 2018).

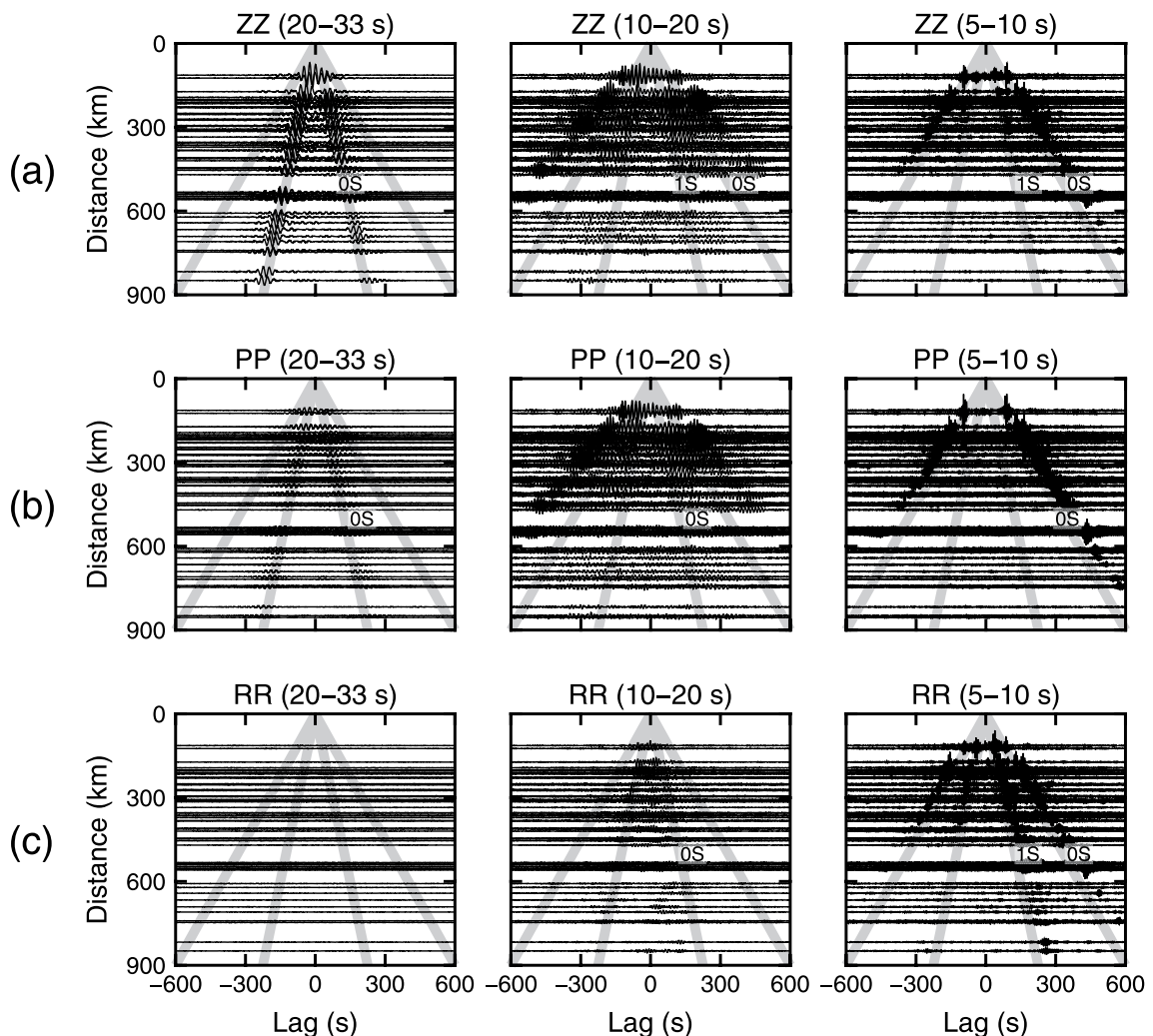


Figure 2. NCFs bandpass filtered at 20–33 s, 10–20 s, and 5–10 s for (a) vertical-vertical (ZZ), (b) pressure-pressure (PP), and (c) radial-radial (RR) component pairs. The gray solid lines indicate arrival times assuming group velocities of 1.5 km/s and 4.0 km/s. All station pairs are shown.

3.2.1. Ambient Noise Analysis

At periods shorter than 25 s, we measure phase velocities of the fundamental and first higher mode Rayleigh waves (0S and 1S modes) via seismic interferometry. Seismic interferometry is a method to extract elastic waves propagating between a pair of stations by calculating noise cross-correlation functions (NCFs), measuring the interstation phase delay of extracted waves (Aki, 1957; Nishida et al., 2008; Shapiro & Campillo, 2004). We calculate NCFs as follows: after dividing whole seismograms into 1600 s-long sections with a 50% overlap, sections that contain glitches and/or earthquake-generated signals are discarded. Then, we stack all the Fourier-transformed sections with spectral whitening (Bensen et al., 2007) and obtain NCFs via the inverse Fourier-transform.

Figure 2 shows NCFs between vertical-vertical (ZZ), pressure-pressure (PP), and radial-radial (RR) components with three different pass bands: 20–33 s, 10–20 s, and 5–10 s. Multiple modes are recognizable: 0S and 1S modes in ZZ- and RR-component NCFs and 0S mode in PP-component NCFs. Some anomalous fast-arriving signals are observable in RR-component NCFs at 10–20 s (Figure 2c). Those signals are not excited by a volcano in Vanuatu reported by Kawano et al. (2020) nor the Aso volcano reported by Kawakatsu et al. (1994) and Zeng and Ni (2010, 2011). They might be seismic signals reflected and/or converted at the seamounts inside of the Oldest-1 Array area (e.g., Takeo et al., 2014).

Considering the possibility that western and eastern areas of the array, which are divided by the seamounts in the middle, have different velocity structures and that the presence of the seamounts might potentially bias the

measurements, we measure phase velocities in each area separately (Figure S1a in Supporting Information S1). We measure phase velocities in the frequency domain by fitting the synthetic cross spectra to the observed real-part of the cross spectra by the multi-mode waveform fitting (Takeo et al., 2014). We only use the real part because the imaginary part results from the inhomogeneous distribution of the noise source (e.g., Harmon et al., 2007; Weaver et al., 2009). If the structure is laterally homogeneous and the ambient noise sources are homogeneously distributed, theoretical cross spectra for 0S and 1S modes in γ -component NCFs ($\gamma = ZZ, PP$, and RR) observed in the l th station pair are given by

$$S_l^{ZZ}(\omega) = a_{0S}^{ZZ}(\omega)J_0\left(\frac{\omega c_{0S}(\omega)}{d_l}\right) + a_{1S}^{ZZ}(\omega)J_0\left(\frac{\omega c_{1S}(\omega)}{d_l}\right), \quad (1)$$

$$S_l^{PP}(\omega) = a_{0S}^{PP}(\omega)J_0\left(\frac{\omega c_{0S}(\omega)}{d_l}\right) + a_{1S}^{PP}(\omega)J_0\left(\frac{\omega c_{1S}(\omega)}{d_l}\right), \quad (2)$$

$$S_l^{RR}(\omega) = a_{0S}^{RR}(\omega)J_{0-2}\left(\frac{\omega c_{0S}(\omega)}{d_l}\right) + a_{1S}^{RR}(\omega)J_{0-2}\left(\frac{\omega c_{1S}(\omega)}{d_l}\right), \quad (3)$$

where $a_{0S}^{\gamma}(\omega)$ and $a_{1S}^{\gamma}(\omega)$ respectively represent source intensity for 0S and 1S modes observed in γ -component NCFs, $c_{0S}(\omega)$ and $c_{1S}(\omega)$ respectively represent phase velocities of 0S and 1S modes, d_l is the great-circle distance between the l th station pair, J_m is the m th order Bessel function of the first kind, and $J_{0-2}(x) = J_0(x) - J_2(x)$. The Love wave contribution in radial components (Aki, 1957) is ignored by assuming that the surface-wave wavelength is shorter than the interstation distances ($c_n(\omega)/\omega \ll d_l$).

Using Equations 1–3, we estimate phase velocities that minimize the squared misfit of all γ -component NCFs between the theoretical ($S_l^{\gamma}(\omega)$) and observed ($\text{Re}[\Phi_l^{\gamma}(\omega)]$) cross spectra. Because the number of available station pairs is limited in this study, we introduce a narrow band smoothing on the estimation of the source intensity, $a_n^{\gamma}(\omega)$, to stabilize the analysis. The smoothing band is defined as from $0.9\omega_0$ (ω_1) to $1.1\omega_0$ (ω_2), where ω_0 is a center frequency. The misfit function is defined as

$$E_{\gamma}(\omega_0) = \frac{\omega_0^{-1} \sum_l^{\omega_2} \sum_{\omega_1}^{\omega_2} \left\{ \text{Re}[\Phi_l^{\gamma}(\omega)] - \hat{S}_l^{\gamma}(\omega; \omega_0) \right\}^2}{\sum_l \left\{ \sum_{\omega_1}^{\omega_2} \Phi_l^{\gamma}(\omega) \right\}^2}, \quad (4)$$

where

$$\hat{S}_l^{\gamma}(\omega; \omega_0) = \hat{a}_{0S}^{\gamma}(\omega_0)J_0\left(\frac{\omega c_{0S}(\omega)}{d_l}\right) + \hat{a}_{1S}^{\gamma}(\omega_0)J_0\left(\frac{\omega c_{1S}(\omega)}{d_l}\right), \quad (5)$$

for $\gamma = ZZ$ and PP and

$$\hat{S}_l^{RR}(\omega; \omega_0) = \hat{a}_{0S}^{RR}(\omega_0)J_{0-2}\left(\frac{\omega c_{0S}(\omega)}{d_l}\right) + \hat{a}_{1S}^{RR}(\omega_0)J_{0-2}\left(\frac{\omega c_{1S}(\omega)}{d_l}\right), \quad (6)$$

for $\gamma = RR$. The source intensity of n th mode in γ -component NCF, $\hat{a}_n^{\gamma}(\omega_0)$, is calculated to minimize the square misfit ($\sum_l \sum_{\omega_1}^{\omega_2} \left\{ \text{Re}[\Phi_l^{\gamma}(\omega)] - \hat{S}_l^{\gamma}(\omega; \omega_0) \right\}^2$). The source intensities are constrained to be non-negative values.

Using the misfit function (Equation 4) that is defined at each frequency for each γ -component, the total misfit function E is given by

$$E = \omega^{-1} \left[2 \sum_{\omega_0} E_{ZZ}(\omega_0) + \sum_{\omega_0} E_{PP}(\omega_0) \right] \text{at } \leq 0.1 \text{ Hz}, \quad (7)$$

$$E = \omega^{-1} \left[\sum_{\omega_0} E_{ZZ}(\omega_0) + \sum_{\omega_0} E_{RR}(\omega_0) + \sum_{\omega_0} E_{PP}(\omega_0) \right] \text{at } > 0.1 \text{ Hz}, \quad (8)$$

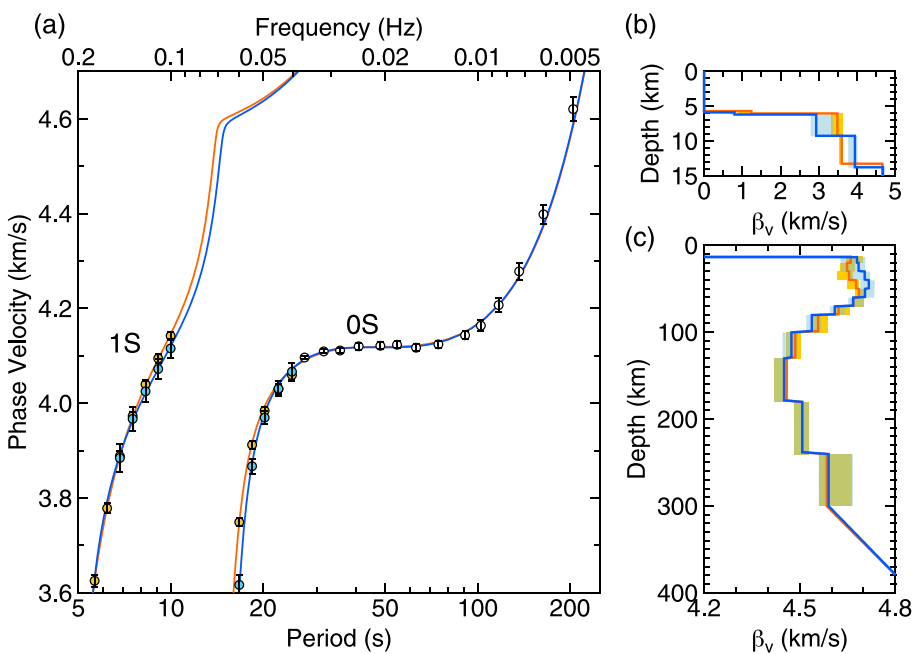


Figure 3. (a) Measured (circles with one-sigma error bars) and modeled (solid lines) average phase velocities. The blue and orange circles are measurements using the stations in the western and eastern areas of the array, respectively. The phase velocities are calculated from the model profiles in (b, c). (b, c) One-dimensional β_v^0 depth profiles focused on the shallow part (b) and the deep part (c). The light shaded areas are the range of model one standard errors.

$$\text{where } w = 3 \sum_{\omega_0} \omega_0^{-1}.$$

The RR-component NCFs at a frequency lower than 0.1 Hz are not used to avoid unknown anomalously fast-arriving signals (Figure 2c). In addition, ZZ-component NCFs are weighted by a factor of two compared to PP-component NCFs; this is because the energy of long-wavelength Rayleigh waves concentrates not in the oceanic layer but in the solid layers and thus appears smaller in the PP component compared to the ZZ component (Figures 2a and 2b; e.g., Takeo et al., 2014). The magnitude of the weight of ZZ-component NCFs in Equation 7 is set to two to keep the number of components the same as short periods.

Due to the limited azimuthal coverage of station pairs, azimuthal anisotropy potentially introduces a bias in the average phase velocity estimate, and the bias can reach up to about 1% (Takeo et al., 2018). We, therefore, simultaneously search for the average (isotropic) and azimuthally variable (anisotropic) phase velocity (Figures 3a and 4) to avoid the bias. We express the phase velocity at each wave-propagation azimuth, θ , as $c(\omega, \theta) = c_{\text{ave}}(\omega)[1 + A_c(\omega)\cos(2\theta) + A_s(\omega)\sin(2\theta)]$, where $c_{\text{ave}}(\omega)$ is the average phase velocity. The amplitude and the fast direction of the azimuthal anisotropy are given by $A(\omega) = \sqrt{[A_c(\omega)]^2 + [A_s(\omega)]^2}$ and $\theta_{\max}(\omega) = \frac{1}{2}\arctan[A_s(\omega)/A_c(\omega)]$, respectively. The 2θ -sinusoidal patterns of azimuthal anisotropy are shown in Figure 4.

Takeo et al. (2014) expressed the dispersion curve as a series of B-spline basis functions. Under this expression, however, unrealistic peaks and/or troughs are potentially introduced to the dispersion curve because of its dependency on the knot intervals. In order to introduce physically realizable constraints on the dispersion curve, we directly calculate the dispersion curves from an isotropic velocity model as for the cases of teleseismic waveforms (e.g., Takeo et al., 2018; Yoshizawa & Kennett, 2002) and the ambient noise on land (Takeo et al., 2022). The model has 14 layers of piecewise constant S-wave velocity from the seafloor to the depth of 190 km. The mantle density and attenuation coefficients are fixed to PREM values (Dziewonski & Anderson, 1981), and a Poisson solid is assumed for the mantle P-wave velocity. Crustal density and P-waves are scaled to S-waves following the relationships used for structural inversions in Takeo et al. (2014). In addition, the parameters for azimuthal anisotropy are assigned for each layer from the seafloor to the depth of 190 km in a similar way.

We estimate the phase velocities that minimize the misfit functions in Equations 7 and 8 by determining the S-wave velocity and parameters for azimuthal anisotropy for each layer using the simulated annealing method

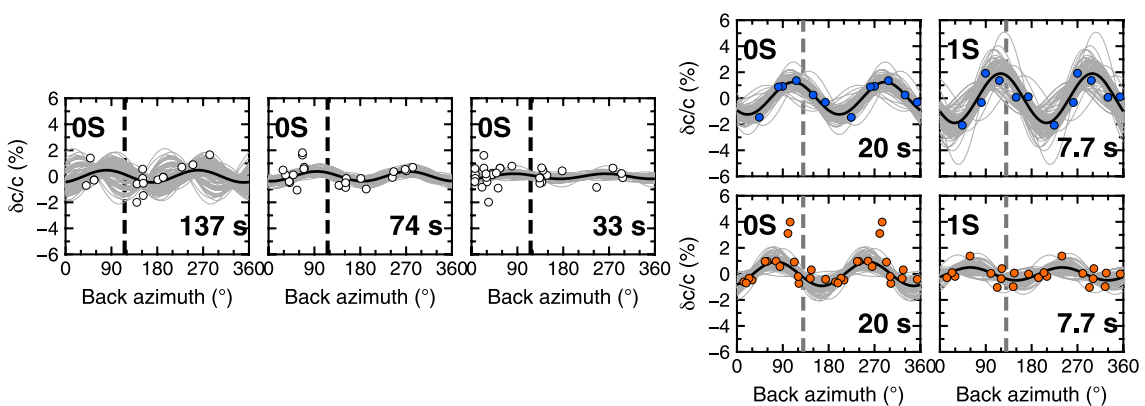


Figure 4. Azimuthal variations of phase velocities relative to their average values (see Figure 3a for average values). The white dots are measurements via teleseismic waveform analysis. The blue and orange dots are measurements via ambient noise analysis. Black solid lines represent 2θ -sinusoidal fittings using the anisotropy model parameters. Gray lines represent one hundred 2θ -sinusoidal model curves estimated from bootstrap method as described in Section 3.2. The black and gray vertical dashed lines represent the absolute plate motion and the past seafloor spreading directions, respectively.

(Nam et al., 2004). In addition, since the short-period 0S- and 1S-mode phase velocities are sensitive to the depth of water and the crustal structures, the thicknesses of those layers are also searched for at each annealing step. For the further analyses in Section 4, we retain only phase-velocity measurements for the final inversion and discard the velocity models that are used for the measurement because we impose weak damping for the velocity modeling at this stage.

The final phase velocities and the standard errors are estimated using the bootstrap method (Efron, 1979). A bootstrap sample consists of randomly selected station pairs of the same data size as the original with duplicates allowed. We estimate 100 bootstrapped dispersion curves ($c_{ave}^1, c_{ave}^2, \dots, c_{ave}^{100}$) of each mode. The average $\bar{c}(\omega)$ and the standard deviation $\Delta c(\omega)$ of those 100 dispersion curves of each mode represent the final phase velocities and the standard errors. The estimation of other parameters and errors ($\bar{A}_c(\omega) \pm \Delta A_c(\omega)$ and $\bar{A}_s(\omega) \pm \Delta A_s(\omega)$) are conducted in a similar way as for the average phase velocities.

3.2.2. Teleseismic Waveform Analysis

In a period range of 25–200 s, we measure phase velocities of the fundamental mode Rayleigh waves in the Oldest-1 Array via teleseismic waveform analysis (Takeo et al., 2018). Since seamounts distort the shallow structure, we consider them to cause a bias in the short-period phase velocity measurements. In order to maximize the number of useable station pairs, we measure phase velocities in three different period bands (Table 1). Station pairs whose paths include seamounts are excluded for measurement at periods shorter than 40 s, but all station pairs are used at longer periods (Figures S1b and S1c in Supporting Information S1). The division of the period band is also effective to increase the number of useable teleseismic events since the observed seismic signal excited by a teleseismic event does not always have large energy in the whole desired period band (25–200 s).

We use teleseismic signals that are excited by earthquakes whose focal depths are shallower than 100 km and moment magnitudes larger than or equal to 5.5 (Figure S2 in Supporting Information S1). The thresholds for the epicentral distance and the signal-to-noise ratio (SNR) are summarized in Table 1. The SNR thresholds depend on the back azimuth because the array is not circular but elliptic. A low (high) SNR threshold is set for events that arrive along the long (short) axis of the array. The signal amplitude is estimated from the peak of the envelop function of the 819 s-long Rayleigh wave. The noise amplitude is estimated from the root-mean-square (RMS) amplitude of the 800 s-long seismograms recorded 2 hr after the origin time of each teleseismic event.

Table 1
Summary of the Analysis at Different Period Bands

Period band (s)	Number of maximum station pairs	Number of events	SNR	Minimum epicentral distance (km)
100–200	55	16	12–30	5,000
40–100	55	24	12–30	5,000
25–40	19	33	3.2–8	4,500

There are two steps in the measurement procedure (Takeo et al., 2013, 2016, 2018). The incident angles of surface waves typically deviate from the great-circle paths due to the heterogeneity outside the array, and the deviation biases the measurement significantly (Foster et al., 2014; Takeo et al., 2013). In the first step, therefore, we simultaneously estimate the incident angle ($\phi_E(\omega)$) and the phase velocity ($c_E(\omega)$) for each event (E) by maximizing the average cross-correlation coefficients (CC_E) defined as

$$CC_E(\omega, c_E, \phi_E) = \frac{1}{N_p} \sum_{j,k} \frac{\sum \Re e \left[F_E^j(\omega) F_E^{*k}(\omega) e^{i\Delta\varphi_E(\omega, c_E, \phi_E)} \right]}{\sqrt{\sum_{\omega} |F_E^j(\omega)|^2} \sqrt{\sum_{\omega} |F_E^{*k}(\omega)|^2}}, \quad (9)$$

where $F_E^j(\omega)$ is the Fourier spectrum of the j th station and N_p is the number of station pairs and an asterisk (*) denotes the complex conjugate. The phase delay, $\Delta\varphi_E(\omega, c_E, \phi_E)$, among station pairs is estimated by assuming the plane-wave-like propagation of surface waves in a local coordinate (Forsyth & Li, 2005; Takeo et al., 2013, 2016). We use station pairs whose CC_E is larger than 0.9 and retain events whose accepted number of station pairs is larger than 10 or 8 for the measurement at periods longer or shorter than 40 s, respectively.

In the second step, we estimate the average phase velocities and their azimuthal variations using all accepted events and the incident angles that are determined in the first step by maximizing the average cross-correlation coefficient (\bar{C}) defined as $\bar{C} = \sum_E N_p CC_E(\omega, \hat{c}_E, \phi_E)$, where $\hat{c}_E = c_{ave}[1 + A_c \cos(2\theta) + A_s \sin(2\theta)]$.

Phase velocities are calculated from an isotropic velocity model in a similar manner as in Section 3.2.1. The model has 12, 16, or 15 layers of a piecewise constant S-wave velocity from depths between 30 and 400 km for the measurements for the long period bands, seafloor and 300 km for intermediate bands, or seafloor and 300 km for short bands, respectively (Table 1). The attenuation coefficients, the density, and P-wave velocities are scaled to S-wave as described in Section 3 (Section 3.2.1). The structure deeper than 400 km is fixed to PREM (Dziewonski & Anderson, 1981). The structure from 300 to 400 km is fixed to ORM (Maggi et al., 2006a) for the measurements at the intermediate and short period bands. The crustal and uppermost mantle structure for the measurements at the long period bands are fixed to the structure that is similar to the final β_V depth profile estimated in Section 4 (Figure S3 in Supporting Information S1). The final average phase velocity and the standard error are calculated in the same manner as in Section 3 (Section 3.2.1). We only retain measured phase velocities for the final inversion in Section 4.

4. Array-Average One-Dimensional Structural Inversion

We model the Rayleigh-wave phase velocities measured by the broadband dispersion analysis in Section 3 to construct array-average S-wave velocity (β_V) profiles for both averaged (C_{ave}) and azimuthally variable ($A_{c,s}$) terms. We describe the azimuthal dependence of β_V as a function of depth z and azimuth θ as $\beta_V(z, \theta) = \beta_V^0(z)[1 + A_c(z)\cos 2\theta + A_s(z)\sin 2\theta]$, where $\beta_V^0(z)$ is the average of β_V that will be referred to as isotropic β_V hereafter, and $A_c(z)$ and $A_s(z)$ are coefficients describing azimuthal anisotropy.

As for the averaged phase velocities (Figure 3a), we follow the method of Takeo et al. (2013, 2016, 2018), and estimate the velocity profile in a depth range from the seafloor to 300 km. The profile has an ocean layer, three crustal layers, and 13 mantle layers. Because the parameters other than β_V^0 are difficult to constrain only using Rayleigh waves, we scale them to β_V^0 as in Section 3 (Section 3.2.1). The total crustal thickness is fixed to 7.6 and 7.9 km respectively for the east and west area, which refer to the results of the P-wave depth profiles of Abrams et al. (1993) (Text S1 and Figure S4 in Supporting Information S1). The thickness of water layer is variable throughout the inversion to account for the shallowest soft sediments. The profile deeper than 400 km is fixed to that of PREM and between 300 and 400 km is linearly interpolated. The anelastic effects are corrected for β_V^0 with the reference frequency of 1 Hz using the attenuation model of PREM. We use the simulated annealing method (Nam et al., 2004) to search for β_V^0 that minimizes a cost function that is comprised of two terms: a misfit term that measures the RMS misfit between the observed and the model phase velocities and a vertical smoothing term (Takeo et al., 2013, 2016). The inverse of one-sigma measurement error is used to weight the data when calculating the RMS misfit.

The model uncertainty is evaluated by the bootstrap method using 100 sets of dispersion curves. Each set of dispersion curves is comprised of the bootstrap resampled 0S- and 1S-mode phase velocities that are obtained

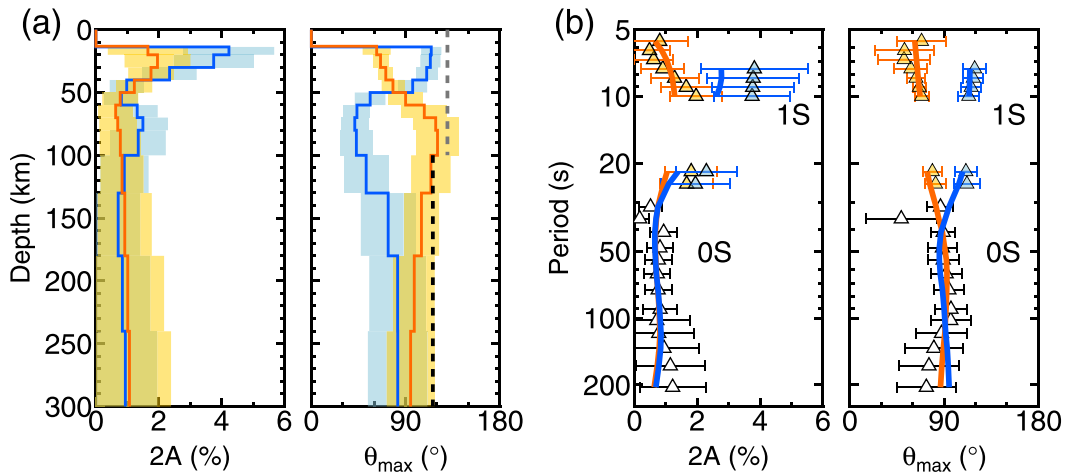


Figure 5. (a) The azimuthally anisotropic model profiles of β_V^0 . The shaded areas represent the one-sigma model uncertainties. The gray and black broken lines respectively represent the direction perpendicular to the 170-Ma isochrone of Seton et al. (2020) and the current absolute plate motion direction. (b) The measurements (triangles with one-sigma error bars) and model predictions (solid lines) of azimuthal anisotropy as a function of frequency in terms of the peak-to-peak amplitude (2A) and the fast direction (θ_{\max}) in the western (blue) and eastern (orange) arrays. Solid lines are predictions calculated from the models in (a).

from ambient noise and/or teleseismic waveform analyses. We obtain 100 β_V^0 profiles from 100 sets of dispersion curves and estimate the average and the standard deviation of those 100 profiles respectively as the final model profile and the model standard error.

As for the azimuthally variable phase velocities (Figures 4 and 5b), we model the azimuthally anisotropic profile in a depth range from the Moho to 300 km. The crust and the structure deeper than 300 km are constrained to be isotropic. The peak-to-peak amplitude of anisotropy corresponds to $2A(z)$ where $A(z) = \sqrt{[A_c(z)]^2 + [A_s(z)]^2}$, and the fast direction of anisotropy is given by $\theta_{\max}(z) = \frac{1}{2}\arctan[A_s(z)/A_c(z)]$. We search for model parameters (A_c and A_s) of azimuthal anisotropy in each of 13 mantle layers that minimize a cost function that consists of an RMS misfit term and a vertical smoothing term (Takeo et al., 2016). As in the case of modeling the isotropic profile, the inverse of one-sigma measurement error is used to weight the data when calculating the RMS misfit. Measurements of the OS mode at periods shorter than 20 s are avoided since the phase velocity in this period band is strongly affected by water depth, making it difficult to extract azimuthal anisotropy. Rayleigh wave azimuthal anisotropy is also affected by P-wave azimuthal anisotropy (e.g., Russell et al., 2019). The pattern of P-wave azimuthal anisotropy shows dominant 2θ patterns for the case of the LPO with the horizontal alignment of a-axes of A-type olivine crystals (Montagner & Nataf, 1986). It is α_H , the horizontally propagating P-wave velocity, that results in such azimuthal anisotropy of Pn-wave observed by refraction studies (e.g., Shinohara et al., 2008). We use the parameter set of α_H , β_V , η_k (Kawakatsu, 2016b) to model the azimuthal anisotropy instead of the conventional parameters α_H , β_V , η (Takeuchi & Saito, 1972) since the conventional η introduces the unpreferable behavior of P-wave kernels that is contaminated by the S-wave sensitivities (Kawakatsu, 2016a; Kawakatsu, 2022; Figure S5 in Supporting Information S1). We constrain α_H anisotropy to be 1.3 times larger than β_V anisotropy by referring to observations in previous refraction study near the array (Shinohara et al., 2008). We further fix η_k as one imposing the elliptic condition, that is, $\eta_k = 1$, for all azimuth directions, which may be justified due to its small value and azimuthal dependency of existing olivine fabrics (Kawakatsu, 2022).

5. Result

5.1. Isotropic Velocity Profile

The estimated isotropic S-wave velocity $\beta_V^0(z)$ profiles in the western and eastern areas of the array are shown in Figures 3b and 3c. Model phase velocities calculated from the final profiles fit the observed data within the one-sigma errors (Figure 3a). There is no significant difference in the mantle between the western and eastern areas since the same dispersion curve is used at periods longer than 25 s to estimate the final profiles. The

velocities in a shallow depth range (<60 km) are ~ 4.7 km/s. The velocity drops at depths below 80 km, reaching below 4.5 km/s in a depth range of 100–240 km, indicating a velocity reduction of $\sim 4\%$. Deeper than a depth of 180 km, the velocity increases to ~ 4.6 km/s in a depth range of 240–300 km. We define the high-velocity part in a depth range of Moho to 60 km as the Lid and the low-velocity part in a depth range of 80–240 km as the low-velocity zone (LVZ). Same as previous studies, we associate the Lid and LVZ as corresponding to the lithosphere and asthenosphere, respectively.

5.2. Azimuthally Anisotropic Profile

Figure 5a shows the azimuthal anisotropy depth profiles of the peak-to-peak amplitude (2A) and the fast direction beneath the Oldest-1 Array. Both the model amplitude and the fast directions fit the data well (Figure 5b). At periods shorter than 10 s, corresponding to the measurements of 1S-mode phase velocities, both the measured amplitude and the fast directions are significantly different between the western and eastern areas of the array (Figure 5b), resulting in a difference at depths shallower than 50 km (Figure 5a). At depths shallower than 50 km, the peak-to-peak amplitude in the west is $2.8 \pm 1.0\%$ on average, while it is $1.6 \pm 0.9\%$ in the east (Figure 5a); in the western area, it changes from 4.3% at Moho to 0.9% at 50 km (Figure 5a), reflecting the change in the corresponding measurement at periods shorter than 10 s and between 20 and 30 s (Figure 5b). The profile of the fast direction is also significantly different between the western and the eastern areas: changing from N115°E and N78°E at Moho to N76°E and N84°E at 50 km depth in the western and eastern areas of the array, respectively. On average, the fast direction is $N109^\circ \pm 11^\circ$ in the west and $N70^\circ \pm 10^\circ$ in the east. Since the direction perpendicular to the 170-Ma isochron is $\sim N130^\circ$ (Seton et al., 2020), the fast directions in both areas deviate from the past seafloor spreading direction, in particular large in the eastern area (Figure 5a).

At depths deeper than 50 km, although the difference of the fast directions at depths of 60–150 km exceeds the one-sigma uncertainty ranges, the difference of azimuthal anisotropy in the western and eastern areas is unlikely to be resolved. This is because the measurements at periods longer than 25 s, where the β_V sensitivities of the OS-mode phase velocity peak at the corresponding depth ranges, are common between the two areas and because the anisotropy amplitude is relatively weak ($\sim 1\%$). Furthermore, a synthetic test indicates that when there is a discontinuous change in azimuthal anisotropy between the shallow and deep depths, the inversion process results in an overshoot of fast-axis at depths below the discontinuity (Figure S6 in Supporting Information S1), suggesting that the separation between the two areas might be a result of the inversion process. In addition, the assumptions in the inversion, such as employing a constant vertical smoothing parameter and fixing the P-S anisotropy scaling at 1.3, may also introduce some bias in the result. We simply note here that within a period range of 25–90 s, where the measurements are robust, the fast direction is about 90° that deviates from the APM direction of N116°E (Gripp & Gordon, 2002).

6. Discussion

6.1. Comparison to the Previous Studies at 130- and 140-Ma Seafloor

Takeo et al. (2018) estimated $\beta_V^0(z)$ profiles beneath two BBOBS arrays in the northwestern Pacific Ocean deployed under the Normal Oceanic Mantle (NOMan) project (Figure 1b). The two arrays are situated in the old normal seafloor of similar ages (NOMan A at 130 Ma and NOMan B at 140 Ma) and separated by $\sim 1,000$ km. They observed the difference in β_V^0 of the LVZ between the two arrays, which were too large to be explained by the cooling due to their age difference. They found that the phase velocity measured at NOMan B was consistent with a half-space cooling (HSC) model for an age of 140 Myrs, whereas the dispersion curve measured at NOMan A was not consistent with the HSC model parameterized for 130 Myrs. Combined with the profile of the azimuthal anisotropy, they interpreted that the bottom of the plate beneath NOMan A was reheated by the upwelling of the small-scale convection and there might be downwelling beneath NOMan B.

We compare the β_V^0 profile of the Oldest-1 Array to those of NOMan A and B of Takeo et al. (2018) (Figure 6a). For the Oldest-1 Array, only the result in the western area is shown. Because we measure phase velocities at longer periods (up to the period of 200 s) for the Oldest-1 Array compared to those (up to 100 s) for NOMan arrays, we resolve structures deeper and constrain the bottom of the LVZ that is recognizable as the velocity increase at depths deeper than 200 km (Figure 6a). β_V^0 profiles of the Lid are similar among the three regions (within the one-sigma uncertainty range), and β_V^0 is ~ 4.7 km/s. The velocity reduction in the LVZ is most prominent in the

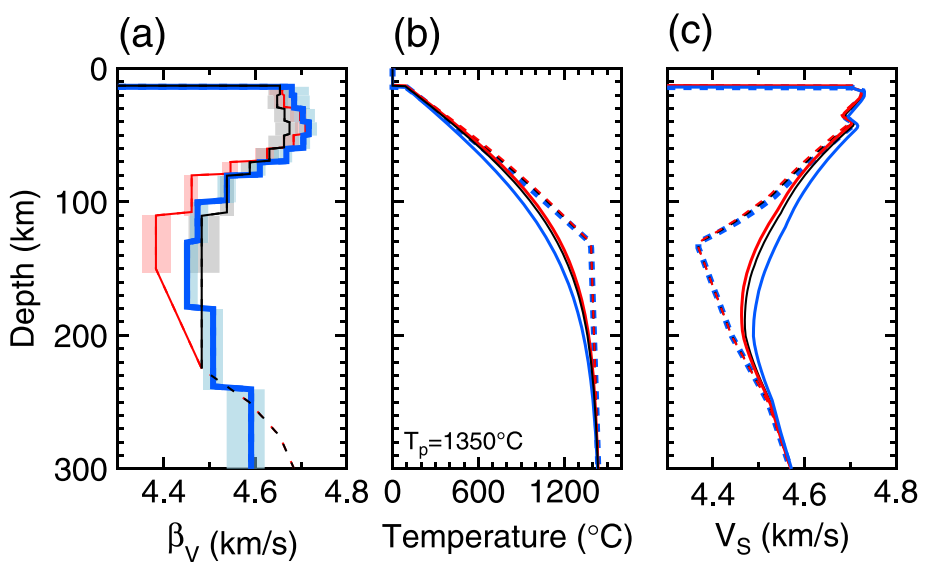


Figure 6. (a) A comparison of β_V profiles estimated at the old Pacific seafloor of 170 Ma (Oldest-1; thick blue line), 140 Ma (NOMan B; thin black line), and 130 Ma (NOMan A; thin red line). The shaded areas represent one-sigma model uncertainties. (b) Temperature profiles of the half-space cooling (HSC; solid lines) and plate cooling (dashed lines) models for 170-Ma (blue), 140-Ma (black), and 130-Ma (red) seafloor. The potential temperature of these models is 1350°C (c) The S-wave velocity depth profiles that correspond to the temperature profiles in (b). The line color scheme is used consistently throughout the figure.

NOMan A (130 Ma), and the velocity reaches a value of less than 4.4 km/s at the depth range of 110–150 km. At the similar depth range of the Oldest-1 and NOMan B, the velocity is similar and ~ 4.5 km/s, indicating that the velocity in the LVZ of the NOMan A is about 1%–2% slower than the other areas.

Figure 6c shows how the age difference might affect the velocity difference among the three areas: we construct temperature profiles of half-space cooling (HSC) model and plate-cooling models for given plate ages. Following Takeo et al. (2018), the potential temperature (T_p) of the ambient mantle is set to 1350°C with an adiabatic temperature gradient of $0.3^\circ\text{C}/\text{km}$ for both models, and the plate thickness is set to 125 km for the plate-cooling model (Parsons & Sclater, 1977). We then convert the temperature profile to an S-wave velocity profile assuming the pyrolite composition model of Stixrude and Lithgow-Bertelloni (2005, 2011). While the plate-cooling model predicts nearly identical temperature and thus velocity profiles for any old oceanic mantle, the HSC model predicts observable variations. Considering the aforementioned finding by Takeo et al. (2018), which indicates the velocity profile of NOMan B can be modeled by the HSC model, we employ the NOMan B profile as a reference in the following discussion.

The age difference of 30 Myrs between Oldest-1 and NOMan B gives a temperature difference of $\sim 50^\circ\text{C}$ at a depth of 150 km for HSC models (Figure 6b), resulting in $\sim 0.6\%$ faster V_s beneath the 170-Ma seafloor than the 140-Ma seafloor (Figure 6c); considering that the observed β_V^0 in Figure 6a is $\sim 0.7\%$ slower (instead of faster) beneath Oldest 1, however, we may conclude that the shear-wave velocity there is $\sim 1.3\%$ slower ($\sim 110^\circ\text{C}$ warmer) than NOMan B at a depth of 150 km if they follow the same half space cooling. A similar argument also indicates that NOMan A is $\sim 1.9\%$ slower ($\sim 160^\circ\text{C}$ warmer) than NOMan B. In this estimation, the effects of premelting or partial melting on seismic attenuation (Havlin et al., 2021; Yamauchi & Takei, 2016) are not considered because the mantle temperature in this region (Figure 6b) is low enough.

6.2. Possible Reheating Beneath the Old Seafloors

The result that the LVZ of Oldest-1 Array is slightly slower than that of NOMan B (Figure 6a), while the age difference predicts significantly faster as discussed in the previous section (Figure 6c), may suggest that the bottom of the Oldest-1 lithosphere is reheated by the small-scale thermal convection (SSC) (e.g., Huang & Zhong, 2005; Korenaga & Jordan, 2004; Richter & Parsons, 1975), which is previously suggested for beneath the NOMan A by Takeo et al. (2018). The SSC transfers heat from the asthenosphere to the bottom of the

lithosphere, and thus reheating will occur at the bottom of the oceanic lithosphere. Following the argument of Takeo et al. (2018), the reheating might be occurring beneath the Oldest-1, but to a lesser extent compared to the NOMan A case.

The estimated depth profile of the azimuthal anisotropy within the asthenosphere shows the peak-to-peak amplitudes of $\sim 1\%$ and the fast directions that deviate from the APM for $\sim 33^\circ$. van Hunen and Čadek (2009) numerically simulated how the SSC perturbed the APM-induced LPO pattern. They showed that the well-developed SSC could randomly disturb the amplitude and the direction of azimuthal anisotropy. When the LPO pattern is spatially smoothed, the amplitude of anisotropy is reduced by a factor of two, while the orientation does not significantly deviate from the APM ($<20^\circ$). Considering the spatial extent of the Oldest-1 Array is $\sim 500 \text{ km} \times 1,000 \text{ km}$ that is significantly larger than the thickness of the LVZ ($\sim 150 \text{ km}$) that may give the spatial scale of the SSC, observations in this study might reflect a smoothed LPO pattern. The peak-to-peak amplitude of the anisotropy in the asthenosphere is smaller than that of NOMan A and B ($\sim 2\%$) by Takeo et al. (2018), which may indicate that degree of disturbance and/or spatially smoothing effect is severer beneath the Oldest-1.

Instead of the ongoing reheating by the SSC, the Oldest-1 and/or the NOMan A mantle might have experienced the rejuvenation in the past (Utada, 2019) that might be related to the Cretaceous volcanic activities. The age of the seamounts near the Oldest-1 Array is $\sim 70\text{--}100 \text{ Ma}$ (Koppers et al., 2003), meaning that there might have been a 30-Myr rejuvenation interval, which coincides with the age difference between the Oldest-1 and NOMan B. The similarity in the β_V^0 profiles between the two regions might indicate that the Oldest-1 mantle has experienced about 30 Myrs of rejuvenation during a period of $\sim 70\text{--}100 \text{ Myrs}$ after the formation of the lithosphere that took place at $\sim 170 \text{ Ma}$.

The compositional heterogeneity is another possibility to explain the difference among three areas. Considering that the crustal structure beneath the Oldest-1 Array is that of the normal oceanic crust (Abrams et al., 1993), the normal oceanic mantle is likely to have been constructed during the crust formation. It is, however, still possible that some alteration processes have occurred in the asthenosphere during the later stage of the evolution.

6.3. Implication for the Evolution of the Infant Pacific Plate

The azimuthal anisotropy at depths shallower than 50 km is significantly different between the western and eastern areas of the array. The fast direction in the west is quasi-perpendicular to the 170-Ma isochron, while the fast direction in the east is not (Figure 7a). The peak-to-peak amplitude of azimuthal anisotropy of the shallowest mantle is $4.3 \pm 1.5\%$ and $1.7 \pm 1.3\%$ beneath the western and eastern areas, respectively. Assuming that Pn anisotropy is 1.3 times larger than Sn anisotropy (Shinohara et al., 2008), the P-wave anisotropy is estimated to be $5.6 \pm 1.9\%$ and $2.1 \pm 1.7\%$ respectively at the top of the upper mantle in the west and the east. The half-spreading rate at the Oldest-1 Array is $\sim 2.3 \text{ cm/year}$ in west and $\sim 3.3 \text{ cm/year}$ in east according to the isochrons (Müller et al., 2019; Seton et al., 2020) (Figure 1a). Compared to the global linear relationship between the Pn-wave azimuthal anisotropy and half-spreading rates (Song & Kim, 2012), which gives ~ 3.5 (west)– ~ 4 (east) % anisotropy, the observed anisotropy of the shallowest mantle beneath the western area is quite large, while the amplitude is quite small in the eastern area.

Although there is no available direct observation of geomagnetic lineation in this region, based on the analyses of the magnetic lineation on the younger seafloor in the northern Pacific (Larson & Chase, 1972; Nakanishi et al., 1992), the Pacific plate is believed to be formed at the Phoenix–Izanagi–Farallon triple junction and thus to have been a triangular shape during its early state (e.g., Seton et al., 2012). In Figure 7a, an ancient RRR triple junction formed by Pacific, Izanagi, and Farallon plates can be recognized as a northernmost corner of a triangle formed by the 180-Ma isochron located at 160°E and 18°N . The NE-SW and NW-SE trending 180-Ma isochrons represent the ancient Pacific–Izanagi and Pacific–Farallon ridges, respectively. The western area is $\sim 500 \text{ km}$ away from the ancient triple junction, whereas the eastern area is in its vicinity. This difference in distance from the ancient triple junction might be the reason for the difference in the observed azimuthal anisotropy. The seafloor away from the triple junction might be formed by relatively simple plate divergence, whereas the seafloor close to the triple junction might have undergone disturbances by mantle upwelling at the triple junction.

In order to test the above-mentioned hypothesis, a simple numerical mantle-flow simulation is performed to examine the seismic azimuthal anisotropy pattern due to the LPO of olivine and enstatite, assuming that the three plates diverge away at an equal rate and equilaterally from an RRR triple junction (Figure 7b), which might

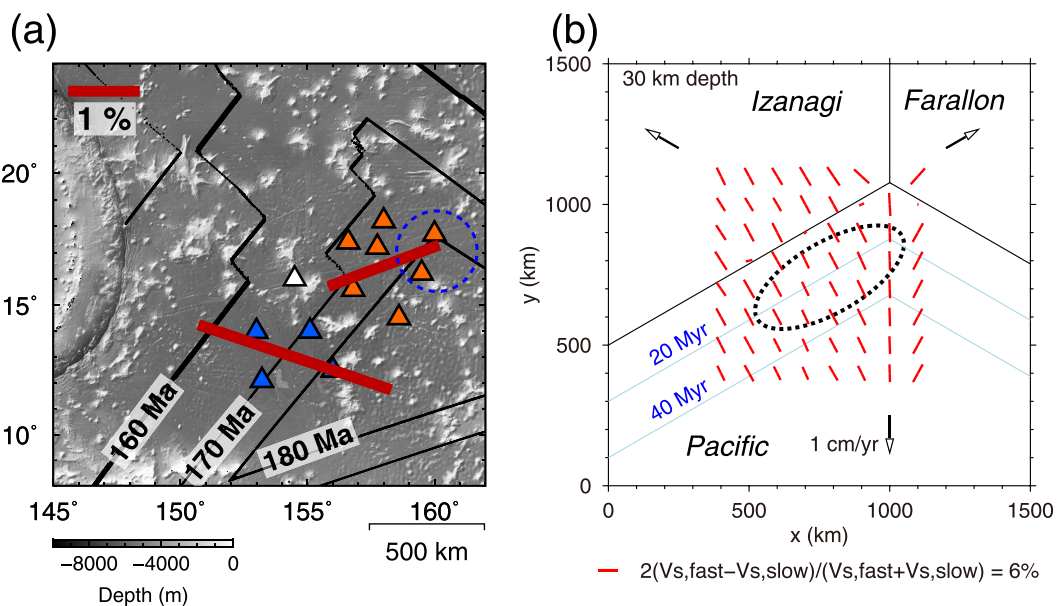


Figure 7. (a) A summary of shallow azimuthal anisotropy measurements. The blue and orange triangles, respectively, represent stations in the western and eastern areas, and the white triangle represent the station that is not used for ambient noise analysis. The red solid bars represent the average of the fast directions from Moho to a depth of 50 km in each area. The length of the bars is proportional to the peak-to-peak amplitude and the 1% scale is shown in the upper left. The blue dashed circle highlights the ancient (180 Ma) RRR triple junction. (b) The simulation results of seismic azimuthal anisotropy at a depth of 30 km. Note that the upper side of the figure is north. The southern, western, and eastern plates represent the Pacific, Izanagi, and Farallon plates, respectively. Black open arrows represent plate-spreading directions, black solid lines represent the ridge axes, sky blue solid lines with age labeled represent the old ridge axes, and red solid bars represent the amplitude and the fast direction of azimuthal anisotropy. The black dotted circle schematically denotes the supposed location of the Oldest-1 Array at 20 Myrs after the spreading began.

represent the situation for the ancient Pacific-Farallon-Izanagi triple junction. The three ridge axes intersect at a point, the triple junction, and passive upwelling is assumed therein. The detail of the simulation is described in Supporting Information S1 (Text S2).

Figure 7b shows the results of the spatial variations of the simulated azimuthal anisotropy. They indicate that the azimuthal anisotropy within the array becomes subparallel to the past seafloor spreading directions regardless of the distance from the triple junction (Figure 7b). This prediction differs from the observations (Figure 7a), suggesting that the mantle dynamics soon after the birth of the Pacific plate might have been more complicated than the assumed simple model. For example, the abrupt change of the isochron (Figure 7a) suggests a possible variation in the spreading rate along the ridge axis at 160–170 Ma. Some studies predict complicated evolutionary processes that involve the change from a ridge-ridge-transform to an RRR triple junction (Boschman & van Hinsbergen, 2016; Handschumacher et al., 1988) rather than a model assumed in the present study that may be regarded as a simplest end-member. Furthermore, the Pacific plate might have frequently drifted and rotated at its early evolution stage, according to the plate reconstruction (Müller et al., 2019; Seton et al., 2020). As observations of the strength and direction of azimuthal anisotropy showing the significant difference between the western and the eastern areas of the Oldest-1 Array, the evolutionary dynamics of the infant Pacific plate might be more complicated than a conventional framework. In order to better understand the evolution history of the infant Pacific plate, observations that cover the rest portion of the oldest seafloor in the western Pacific might be useful.

Alternatively, the observed azimuthal anisotropy may not entirely represent the evolution dynamics of the infant Pacific plate, but a result of disturbances associated with subsequent volcanic activities. Pacific plate had experienced volcanic activity during the Cretaceous, which emplaced many LIP (large igneous province) products in the western Pacific basin (Coffin et al., 2006). The wide LIP products covering the Oldest-1 Array area were formed by ocean basin flood basalt (Abrams et al., 1993; Coffin & Eldholm, 1994), which less alters the pre-existing crust compared to the formation of off-axis oceanic plateaus (Coffin et al., 2006). More details of the evolutionary history of the Pacific plate might be unraveled if the entire region of the oldest Pacific plate is imaged by future observations.

7. Conclusion

We measure Rayleigh-wave dispersions in a period range of 5–200 s using seismograms recorded at the oldest (170–180 Ma) Pacific seafloor. At short periods (<25 s), we measure phase velocities of the fundamental and first higher mode Rayleigh waves (0S and 1S) by ambient noise analysis. At long periods (>25 s), we measure the 0S-mode phase velocities by teleseismic waveform analysis. We then invert the broadband phase velocities for one-dimensional isotropic and azimuthally anisotropic shear-wave velocity profiles in a depth range from crust to 300 km to discuss the lithosphere–asthenosphere system beneath the oldest Pacific seafloor. The high-velocity Lid (<60 km) and the underlying low-velocity zone (LVZ) (80–240 km) are well-resolved in the isotropic velocity model with a velocity difference of ~4%. The shear-wave depth profile is further compared to those obtained at 130- (NOMan A) and 140-Ma (NOMan B) seafloors. The LVZ of the Oldest-1 Array appears ~1.3% slower (~110°C warmer) than that of NOMan B after the temperature correction of seafloor age difference based on the half-space cooling model, suggesting the occurrence of some reheating process beneath the oldest lithosphere. In the azimuthally anisotropic structure, the difference between the western and the eastern areas of the Oldest-1 Array at depths shallower than 50 km is well-resolved: the peak-to-peak amplitude (2A) is ~2.8% and the fast direction (θ_{\max}) is quasi-parallel to the past seafloor spreading direction in the western area of the array, whereas 2A is ~1.6% and θ_{\max} largely deviates from the past seafloor spreading direction in the eastern area of the array. At depths deeper than 50 km, 2A is weak (~1%), and θ_{\max} is oblique from the absolute plate motion direction. The azimuthal anisotropy in depths shallower than 50 km may reflect the dynamics of the birth of the Pacific plate.

Data Availability Statement

The Oldest-1 Array data set will be available from the Ocean Hemisphere Project Data Management Center (OHPDMC; directly access from <http://ohpdmc.eri.u-tokyo.ac.jp/dataset/campaign/obs/index.html>). The data will be released to the public on 1 September 2023 after the moratorium period. Figures are plotted using the Generic Mapping Tools (www.soest.hawaii.edu/gmt; Wessel et al., 2013).

Acknowledgments

We thank the captains and crews of R/V ISABU and R/V ONNURI of KIOST for the deployment and recovery cruises. The authors thank L. Worthington, J. Russell, and an anonymous reviewer for constructive reviews to improve the article. Y. Kawano is supported by the KAKENHI Grant-in-Aid for JSPS Fellows (JP20J11260) from the JSPS. This work is supported by JSPS KAKENHI Grants 18H03735, 21H04504, and 22H01330, and Japan-Korea Basic Scientific Cooperation Program between JSPS and NRF, Grant JPJSBP120218807. Y. Kim and S-M. Lee acknowledge fundings from Korea Institute of Ocean Science and Technology (PE99656 and PE99796) and also from NRF (2022R1A5A1085103).

References

- Abrams, L., Larson, R., Shipley, T., & Lancelot, Y. (1993). Cretaceous volcanic sequences and Jurassic oceanic crust in the East Mariana and Pigafetta basins of the Western Pacific. In M. S. Pringle, W. W. Sager, W. V. Sliter, & S. Stein (Eds.), *The Mesozoic Pacific: Geology, tectonics, and volcanism*, Geophysical Monograph Series (Vol. 77, pp. 77–101). American Geophysical Union.
- Aki, K. (1957). Space and time spectra of stationary stochastic waves, with special reference to microtremors. *Bulletin of the Earthquake Research Institute*, 35, 415–456.
- Bell, S. W., Forsyth, D. W., & Ruan, Y. (2015). Removing noise from the vertical component records of ocean-bottom seismometers: Results from year one of the Cascadia Initiative. *Bulletin of the Seismological Society of America*, 105(1), 300–313. <https://doi.org/10.1785/0120140054>
- Bensen, G., Ritzwoller, M., Barmin, M., Levshin, A. L., Lin, F., Moschetti, M., et al. (2007). Processing seismic ambient noise data to obtain reliable broad-band surface wave dispersion measurements. *Geophysical Journal International*, 169(3), 1239–1260. <https://doi.org/10.1111/j.1365-246X.2007.03374.x>
- Boschman, L. M., & van Hinsbergen, D. J. (2016). On the enigmatic birth of the Pacific plate within the Panthalassa Ocean. *Science Advances*, 2(7), e1600022. <https://doi.org/10.1126/sciadv.1600022>
- Burgos, G., Montagner, J., Beucler, E., Capdeville, Y., Mocquet, A., & Drilleau, M. (2014). Oceanic lithosphere–asthenosphere boundary from surface wave dispersion data. *Journal of Geophysical Research: Solid Earth*, 119(2), 1079–1093. <https://doi.org/10.1002/2013JB010528>
- Coffin, M. F., Duncan, R. A., Eldholm, O., Fitton, J. G., Frey, F. A., Larsen, H. C., et al. (2006). Large igneous provinces and scientific ocean drilling: Status quo and a look ahead. *Oceanography*, 19(4), 150–160. <https://doi.org/10.5670/oceanog.2006.13>
- Coffin, M. F., & Eldholm, O. (1994). Large igneous provinces: Crustal structure, dimensions, and external consequences. *Review of Geophysics*, 32(1), 1–36. <https://doi.org/10.1029/93RG02508>
- Crawford, W. C., & Webb, S. C. (2000). Identifying and removing tilt noise from low-frequency (<0.1 Hz) seafloor vertical seismic data. *Bulletin of the Seismological Society of America*, 90(4), 952–963. <https://doi.org/10.1785/0119990121>
- Dorman, J., Ewing, M., & Oliver, J. (1960). Study of shear-velocity distribution in the upper mantle by mantle Rayleigh waves. *Bulletin of the Seismological Society of America*, 50(1), 87–115.
- Dziewonski, A. M., & Anderson, D. L. (1981). Preliminary reference Earth model. *Physics of the Earth and Planetary Interiors*, 25(4), 297–356. [https://doi.org/10.1016/0031-9201\(81\)90046-7](https://doi.org/10.1016/0031-9201(81)90046-7)
- Efron, B. (1979). Bootstrap methods: Another look at the jackknife. *Annals of Statistics*, 7(1), 1–26. <https://doi.org/10.1214/aos/1176344552>
- Eilon, Z. C., Zhang, L., Gaherty, J. B., Forsyth, D. W., & Russell, J. B. (2022). Sub-lithospheric small-scale convection tomographically imaged beneath the Pacific plate. *Geophysical Research Letters*, 49(18), e2022GL100351. <https://doi.org/10.1029/2022GL100351>
- Forsyth, D. W. (1975). The early structural evolution and anisotropy of the oceanic upper mantle. *Geophysical Journal International*, 43(1), 103–162. <https://doi.org/10.1111/j.1365-246X.1975.tb00630.x>
- Forsyth, D. W., & Li, A. (2005). Array analysis of two-dimensional variations in surface wave phase velocity and azimuthal anisotropy in the presence of multipathing interference. In A. Levander & G. Nolet (Eds.), *Seismic Earth: Array analysis of broadband seismograms*, Geophysical Monograph Series (Vol. 157, pp. 81–97). American Geophysical Union.
- Foster, A., Ekström, G., & Hjörleifsdóttir, V. (2014). Arrival-angle anomalies across the USArray transportable array. *Earth and Planetary Science Letters*, 402, 58–68. <https://doi.org/10.1016/j.epsl.2013.12.046>

- Gripp, A. E., & Gordon, R. G. (2002). Young tracks of hotspots and current plate velocities. *Geophysical Journal International*, 150(2), 321–361. <https://doi.org/10.1046/j.1365-246X.2002.01627.x>
- Gutenberg, B. (1948). On the layer of relatively low wave velocity at a depth of about 80 kilometers. *Bulletin of the Seismological Society of America*, 38(2), 121–148. <https://doi.org/10.1785/bssa0380020121>
- Gutenberg, B., & Richter, C. F. (1939). New evidence for a change in physical conditions at depths near 100 kilometers. *Bulletin of the Seismological Society of America*, 29(4), 531–537. <https://doi.org/10.1785/BSSA0290040531>
- Handscombacher, D. W., Sager, W. W., Hilde, T. W., & Bracey, D. R. (1988). Pre-Cretaceous tectonic evolution of the Pacific plate and extension of the geomagnetic polarity reversal time scale with implications for the origin of the Jurassic “Quiet Zone”. *Tectonophysics*, 155(1–4), 365–380. [https://doi.org/10.1016/0040-1951\(88\)90275-2](https://doi.org/10.1016/0040-1951(88)90275-2)
- Harmon, N., Forsyth, D., & Webb, S. (2007). Using ambient seismic noise to determine short-period phase velocities and shallow shear velocities in young oceanic lithosphere. *Bulletin of the Seismological Society of America*, 97(6), 2009–2023. <https://doi.org/10.1785/0120070050>
- Havlin, C., Holtzman, B. K., & Hopper, E. (2021). Inference of thermodynamic state in the asthenosphere from anelastic properties, with applications to North American upper mantle. *Physics of the Earth and Planetary Interiors*, 314, 106639. <https://doi.org/10.1016/j.pepi.2020.106639>
- Hess, H. (1964). Seismic anisotropy of the uppermost mantle under oceans. *Nature*, 203(4945), 629–631. <https://doi.org/10.1038/2036290>
- Huang, J., & Zhong, S. (2005). Sublithospheric small-scale convection and its implications for the residual topography at old ocean basins and the plate model. *Journal of Geophysical Research*, 110(B5), B05404. <https://doi.org/10.1029/2004JB003153>
- Kaneda, K., Kodaira, S., Nishizawa, A., Morishita, T., & Takahashi, N. (2010). Structural evolution of preexisting oceanic crust through intraplate igneous activities in the Marcus-Wake seamount chain. *Geochemistry, Geophysics, Geosystems*, 11(10). <https://doi.org/10.1029/2010GC003231>
- Karato, S., Jung, H., Katayama, I., & Skemer, P. (2008). Geodynamic significance of seismic anisotropy of the upper mantle: New insights from laboratory studies. *Annual Review of Earth and Planetary Sciences*, 36(1), 59–95. <https://doi.org/10.1146/annurev.earth.36.031207.124120>
- Kawakatsu, H. (2016a). A new fifth parameter for transverse isotropy II: Partial derivatives. *Geophysical Journal International*, 206(1), 360–367. <https://doi.org/10.1093/gji/ggw152>
- Kawakatsu, H. (2016b). A new fifth parameter for transverse isotropy. *Geophysical Journal International*, 204(1), 682–685. <https://doi.org/10.1093/gji/ggv479>
- Kawakatsu, H. (2022). On the sensitivity kernels for Rayleigh wave azimuthal anisotropy. Programme and abstracts the Seismological Society of Japan 2022 Fall Meeting, S01-14. Retrieved from <https://www.zisin.jp/publications/lecture.html>
- Kawakatsu, H., Ohminato, T., & Ito, H. (1994). 10s-period volcanic tremors observed over a wide area in southwestern Japan. *Geophysical Research Letters*, 21(18), 1963–1966. <https://doi.org/10.1029/94GL01683>
- Kawano, Y., Isse, T., Kawakatsu, H., Shiobara, H., Takeuchi, N., Sugioka, H., et al. (2023). Noise reduction from vertical component seismograms recorded by broadband ocean bottom seismometers deployed at the Western Pacific. *Bulletin of the Seismological Society of America*, XX, 1–13. <https://doi.org/10.1785/0120220256>
- Kawano, Y., Isse, T., Takeo, A., Kawakatsu, H., Suetsugu, D., Shiobara, H., et al. (2020). Persistent long-period signals recorded by an OBS array in the Western-Central Pacific: Activity of Ambrym volcano in Vanuatu. *Geophysical Research Letters*, 47(19), e2020GL089108. <https://doi.org/10.1029/2020GL089108>
- Koppers, A. A., Staudigel, H., Pringle, M. S., & Wijbrans, J. R. (2003). Short-lived and discontinuous intraplate volcanism in the South Pacific: Hot spots or extensional volcanism? *Geochemistry, Geophysics, Geosystems*, 4(10). <https://doi.org/10.1029/2003GC000533>
- Korenaga, J., & Jordan, T. H. (2004). Physics of multiscale convection in Earth's mantle: Evolution of sublithospheric convection. *Journal of Geophysical Research*, 109(B1). <https://doi.org/10.1029/2003jb002464>
- Korenaga, T., Korenaga, J., Kawakatsu, H., & Yamano, M. (2021). A new reference model for the evolution of oceanic lithosphere in a cooling Earth. *Journal of Geophysical Research: Solid Earth*, 126(6), e2020JB021528. <https://doi.org/10.1029/2020JB021528>
- Larson, R. L., & Chase, C. G. (1972). Late Mesozoic evolution of the Western Pacific Ocean. *Geological Society of America Bulletin*, 83(12), 3627–3644. [https://doi.org/10.1130/0016-7606\(1972\)83\[3627:LMEOTW\]2.0.CO;2](https://doi.org/10.1130/0016-7606(1972)83[3627:LMEOTW]2.0.CO;2)
- Lin, P. P., Gaherty, J. B., Jin, G., Collins, J. A., Lizarralde, D., Evans, R., & Hirth, G. (2016). High-resolution seismic constraints on flow dynamics in the oceanic asthenosphere. *Nature*, 535(7613), 538–541. <https://doi.org/10.1038/nature18012>
- Maggi, A., Debayle, E., Priestley, K., & Barrool, G. (2006a). Multimode surface waveform tomography of the Pacific Ocean: A closer look at the lithospheric cooling signature. *Geophysical Journal International*, 166(3), 1384–1397. <https://doi.org/10.1111/j.1365-246X.2006.03037.x>
- Maggi, A., Debayle, E., Priestley, K., & Barrool, G. (2006b). Azimuthal anisotropy of the Pacific region. *Earth and Planetary Science Letters*, 250(1–2), 53–71. <https://doi.org/10.1016/j.epsl.2006.07.010>
- Mark, H. F., Lizarralde, D., Collins, J. A., Miller, N. C., Hirth, G., Gaherty, J. B., & Evans, R. L. (2019). Azimuthal seismic anisotropy of 70-Ma Pacific-plate upper mantle. *Journal of Geophysical Research: Solid Earth*, 124(2), 1889–1909. <https://doi.org/10.1029/2018JB016451>
- Montagner, J., & Nataf, H. (1986). A simple method for inverting the azimuthal anisotropy of surface waves. *Journal of Geophysical Research*, 91(B1), 511–520. <https://doi.org/10.1029/JB091iB01p00511>
- Müller, R. D., Zahirovic, S., Williams, S. E., Cannon, J., Seton, M., Bower, D. J., et al. (2019). A global plate model including lithospheric deformation along major rifts and orogens since the Triassic. *Tectonics*, 38(6), 1884–1907. <https://doi.org/10.1029/2018TC005462>
- Nakanishi, M., Tamaki, K., & Kobayashi, K. (1992). Magnetic anomaly lineations from Late Jurassic to Early Cretaceous in the west-central Pacific Ocean. *Geophysical Journal International*, 109(3), 701–719. <https://doi.org/10.1111/j.1365-246X.1992.tb00126.x>
- Nam, D., Lee, J., & Park, C. H. (2004). n-dimensional Cauchy neighbor generation for the fast simulated annealing. *IEICE - Transactions on Info and Systems*, 87(11), 2499–2502.
- Nicolas, A., & Christensen, N. I. (1987). Formation of anisotropy in upper mantle peridotites-A review. In K. Fuchs & C. Froidevaux (Eds.), *Composition, structure and dynamics of the lithosphere-asthenosphere system*, Geodynamics Series (Vol. 16, pp. 111–123). American Geophysical Union.
- Nishida, K., Kawakatsu, H., & Obara, K. (2008). Three-dimensional crustal S wave velocity structure in Japan using microseismic data recorded by Hi-net tiltmeters. *Journal of Geophysical Research*, 113(B10), B10302. <https://doi.org/10.1029/2007JB005395>
- Nishimura, C. E., & Forsyth, D. W. (1989). The anisotropic structure of the upper mantle in the Pacific. *Geophysical Journal International*, 96(2), 203–229. <https://doi.org/10.1111/j.1365-246X.1989.tb04446.x>
- Parker, R., & Oldenburg, D. (1973). Thermal model of ocean ridges. *Nature; Physical Science*, 242(122), 137–139. <https://doi.org/10.1038/physci242137a0>
- Parsons, B., & McKenzie, D. (1978). Mantle convection and the thermal structure of the plates. *Journal of Geophysical Research*, 83(B9), 4485–4496. <https://doi.org/10.1029/jb083ib09p04485>
- Parsons, B., & Sclater, J. G. (1977). An analysis of the variation of ocean floor bathymetry and heat flow with age. *Journal of Geophysical Research*, 82(5), 803–827. <https://doi.org/10.1029/JB082i005p00803>

- Richter, F. M., & Parsons, B. (1975). On the interaction of two scales of convection in the mantle. *Journal of Geophysical Research*, 80(17), 2529–2541. <https://doi.org/10.1029/JB080i017p02529>
- Russell, J. B. (2021). *Structure and evolution of the oceanic lithosphere-asthenosphere system from high-resolution surface-wave imaging*. (Doctoral dissertation). Columbia University. <https://doi.org/10.7916/d8-33w6-f908>
- Russell, J. B., Gaherty, J. B., Lin, P. P., Lizarralde, D. J., Collins, A., Hirth, G., & Evans, R. L. (2019). High-resolution constraints on Pacific upper mantle petrofabric inferred from surface-wave anisotropy. *Journal of Geophysical Research: Solid Earth*, 124(1), 631–657. <https://doi.org/10.1029/2018JB016598>
- Seton, M., Müller, R. D., Zahirovic, S., Gaina, C., Torsvik, T., Shephard, G., et al. (2012). Global continental and ocean basin reconstructions since 200 Ma. *Earth-Science Reviews*, 113(3–4), 212–270. <https://doi.org/10.1016/j.earscirev.2012.03.002>
- Seton, M., Müller, R. D., Zahirovic, S., Williams, S., Wright, N. M., Cannon, J., et al. (2020). A global data set of present-day oceanic crustal age and seafloor spreading parameters. *Geochemistry, Geophysics, Geosystems*, 21(10), e2020GC009214. <https://doi.org/10.1029/2020GC009214>
- Shapiro, N. M., & Campillo, M. (2004). Emergence of broadband Rayleigh waves from correlations of the ambient seismic noise. *Geophysical Research Letters*, 31(7). <https://doi.org/10.1029/2004GL019491>
- Shinohara, M., Fukano, T., Kanazawa, T., Araki, E., Suyehiro, K., Mochizuki, M., et al. (2008). Upper mantle and crustal seismic structure beneath the Northwestern Pacific Basin using a seafloor borehole broadband seismometer and ocean bottom seismometers. *Physics of the Earth and Planetary Interiors*, 170(1–2), 95–106. <https://doi.org/10.1016/j.pepi.2008.07.039>
- Shintaku, N., Forsyth, D. W., Hajewski, C. J., & Weeraratne, D. S. (2014). Pn anisotropy in Mesozoic Western Pacific lithosphere. *Journal of Geophysical Research: Solid Earth*, 119(4), 3050–3063. <https://doi.org/10.1002/2013JB010534>
- Song, T. A., & Kim, Y. (2012). Anisotropic uppermost mantle in young subducted slab underplating Central Mexico. *Nature Geoscience*, 5(1), 55–59. <https://doi.org/10.1038/ngeo1342>
- Stadler, T. J., & Tominaga, M. (2015). Intraplate volcanism of the Western Pacific: New insights from geological and geophysical observations in the Pigafetta Basin. *Geochemistry, Geophysics, Geosystems*, 16(9), 3015–3033. <https://doi.org/10.1002/2015GC005873>
- Stein, C. A., & Stein, S. (1992). A model for the global variation in oceanic depth and heat flow with lithospheric age. *Nature*, 359(6391), 123–129. <https://doi.org/10.1038/359123a0>
- Stixrude, L., & Lithgow-Bertelloni, C. (2005). Mineralogy and elasticity of the oceanic upper mantle: Origin of the low-velocity zone. *Journal of Geophysical Research*, 110(B3), B03204. <https://doi.org/10.1029/2004JB002965>
- Stixrude, L., & Lithgow-Bertelloni, C. (2011). Thermodynamics of mantle minerals - II. Phase equilibria. *Geophysical Journal International*, 184(3), 1180–1213. <https://doi.org/10.1111/j.1365-246X.2010.04890.x>
- Takeo, A., Forsyth, D. W., Weeraratne, D. S., & Nishida, K. (2014). Estimation of azimuthal anisotropy in the NW Pacific from seismic ambient noise in seafloor records. *Geophysical Journal International*, 199(1), 11–22. <https://doi.org/10.1093/gji/ggu240>
- Takeo, A., Kawakatsu, H., Isse, T., Nishida, K., Shiobara, H., Sugioka, H., et al. (2018). In situ characterization of the lithosphere-asthenosphere system beneath NW Pacific Ocean via broadband dispersion survey with two OBS arrays. *Geochemistry, Geophysics, Geosystems*, 19(9), 3529–3539. <https://doi.org/10.1029/2018GC007588>
- Takeo, A., Kawakatsu, H., Isse, T., Nishida, K., Sugioka, H., Ito, A., et al. (2016). Seismic azimuthal anisotropy in the oceanic lithosphere and asthenosphere from broadband surface wave analysis of OBS array records at 60 Ma seafloor. *Journal of Geophysical Research: Solid Earth*, 121(3), 1927–1947. <https://doi.org/10.1002/2015JB012429>
- Takeo, A., Nishida, K., Aoyama, H., Ishise, M., Kai, T., Kurihara, R., et al. (2022). S-wave modelling of the Showa-Shinzan lava dome in Usu Volcano, Northern Japan, from seismic observations. *Geophysical Journal International*, 230(3), 1662–1678. <https://doi.org/10.1093/gji/gjac111>
- Takeo, A., Nishida, K., Isse, T., Kawakatsu, H., Shiobara, H., Sugioka, H., & Kanazawa, T. (2013). Radially anisotropic structure beneath the Shikoku Basin from broadband surface wave analysis of ocean bottom seismometer records. *Journal of Geophysical Research: Solid Earth*, 118(6), 2878–2892. <https://doi.org/10.1002/jgrb.50219>
- Takeuchi, H., & Saito, M. (1972). Seismic surface waves. In B. A. Bolt (Ed.), *Method in computational physics: Advances in research and applications* (Vol. 11, pp. 217–295). Academic Press.
- Toomey, D. R., Jousselin, D., Dunn, R. A., Wilcock, W. S., & Detrick, R. (2007). Skew of mantle upwelling beneath the East Pacific Rise governs segmentation. *Nature*, 446(7134), 409–414. <https://doi.org/10.1038/nature05679>
- Utada, H. (2019). Ocean bottom geophysical array studies may reveal the cause of seafloor flattening. *Earth and Planetary Science Letters*, 518, 100–107. <https://doi.org/10.1016/j.epsl.2019.04.040>
- van Hunen, J., & Čadek, O. (2009). Reduced oceanic seismic anisotropy by small-scale convection. *Earth and Planetary Science Letters*, 284(3–4), 622–629. <https://doi.org/10.1016/j.epsl.2009.05.034>
- Weaver, R., Froment, B., & Campillo, M. (2009). On the correlation of non-isotropically distributed ballistic scalar diffuse waves. *Journal of the Acoustical Society of America*, 126(4), 1817–1826. <https://doi.org/10.1121/1.3203359>
- Wessel, P., Smith, W. H., Scharrroo, R., Luis, J., & Wobbe, F. (2013). Generic mapping tools: Improved version released. *Eos, Transactions American Geophysical Union*, 94(45), 409–410. <https://doi.org/10.1029/2013EO450001>
- White, R. S., McKenzie, D., & O’Nions, R. K. (1992). Oceanic crustal thickness from seismic measurements and rare earth element inversions. *Journal of Geophysical Research*, 97(B13), 19683–19715. <https://doi.org/10.1029/92JB01749>
- Yamauchi, H., & Takei, Y. (2016). Polycrystal anelasticity at near-solidus temperatures. *Journal of Geophysical Research: Solid Earth*, 121(11), 7790–7820. <https://doi.org/10.1002/2016JB013316>
- Yang, X., Luo, Y., Xu, H., & Zhao, K. (2020). Shear wave velocity and radial anisotropy structures beneath the central Pacific from surface wave analysis of OBS records. *Earth and Planetary Science Letters*, 534, 116086. <https://doi.org/10.1016/j.epsl.2020.116086>
- Yoshizawa, K., & Kennett, B. (2002). Non-linear waveform inversion for surface waves with a neighbourhood algorithm—Application to multi-mode dispersion measurements. *Geophysical Journal International*, 149(1), 118–133. <https://doi.org/10.1046/j.1365-246X.2002.01634.x>
- Zeng, X., & Ni, S. (2010). A persistent localized microseismic source near the Kyushu Island, Japan. *Geophysical Research Letters*, 37(24). <https://doi.org/10.1029/2010GL045774>
- Zeng, X., & Ni, S. (2011). Correction to “A persistent localized microseismic source near the Kyushu Island, Japan”. *Geophysical Research Letters*, 38(16), L16320. <https://doi.org/10.1029/2011GL048822>

References From the Supporting Information

- Kaminski, E., Ribe, N. M., & Browaeys, J. T. (2004). D-Rex, a program for calculation of seismic anisotropy due to crystal lattice preferred orientation in the convective upper mantle. *Geophysical Journal International*, 158(2), 744–752. <https://doi.org/10.1111/j.1365-246X.2004.02308.x>
- Morishige, M., & Honda, S. (2011). Three-dimensional structure of P-wave anisotropy in the presence of small-scale convection in the mantle wedge. *Geochemistry, Geophysics, Geosystems*, 12(12). <https://doi.org/10.1029/2011GC003866>
- Morishige, M., & Honda, S. (2013). Mantle flow and deformation of subducting slab at a plate junction. *Earth and Planetary Science Letters*, 365, 132–142. <https://doi.org/10.1016/j.epsl.2013.01.033>
- Shen, Y., & Forsyth, D. W. (1992). The effects of temperature- and pressure-dependent viscosity on three-dimensional passive flow of the mantle beneath a ridge-transform system. *Journal of Geophysical Research*, 97(B13), 19717–19728. <https://doi.org/10.1029/92JB01467>